
Article:
Beola, Lilianne, Asín, Laura, Roma-Rodrigues, Catarina et al. (10 more authors) (2020) The intracellular number of magnetic nanoparticles modulates the apoptotic death pathway after magnetic hyperthermia treatment. ACS Applied Materials and Interfaces. pp. 43474-43487. ISSN 1944-8252

https://doi.org/10.1021/acsami.0c12900

Intracellular number of magnetic nanoparticles modulates the apoptotic death pathway after magnetic hyperthermia treatment

*Lilianne Beola,[±] Laura Asín,[±,≠,] * Catarina Roma-Rodrigues,[¥] Yilian Fernández-Afonso,[±] Raluca M. Fratila,[±,≠] David Serantes,[†] Sergiu Ruta,[‡] Roy W. Chantrell,[‡] Alexandra R. Fernandes,[¥] Pedro V. Baptista,[¥] Jesús M. de la Fuente,[±,≠] Valeria Grazú,[±,≠] Lucía Gutiérrez[±,≠ #,*]*

[±]Instituto de Nanociencia y Materiales de Aragón (INMA), CSIC-Universidad de Zaragoza, 50009 Zaragoza, Spain.

[≠]Centro de Investigación Biomédica en Red de Bioingeniería, Biomateriales y Nanomedicina (CIBER-BBN), 50009 Zaragoza, Spain.

[#]Department of Analytical Chemistry, Universidad de Zaragoza, Edificio I+D, 50018 Zaragoza, Spain.

[¥]UCIBIO, Departamento de Ciências da Vida, Faculdade de Ciências e Tecnologia, Universidade Nova de Lisboa, Campus da Caparica, 2829-516 Caparica, Portugal.

†Applied Physics Department and Instituto de Investigacións Tecnolóxicas, Universidade de Santiago de Compostela, 15782 Santiago de Compostela, Spain.

‡Department of Physics, University of York, Heslington, YO10 5DD, York, United Kingdom.

L.A.: lasin@unizar.es; L.G.: lu@unizar.es

Table of contents graphic:

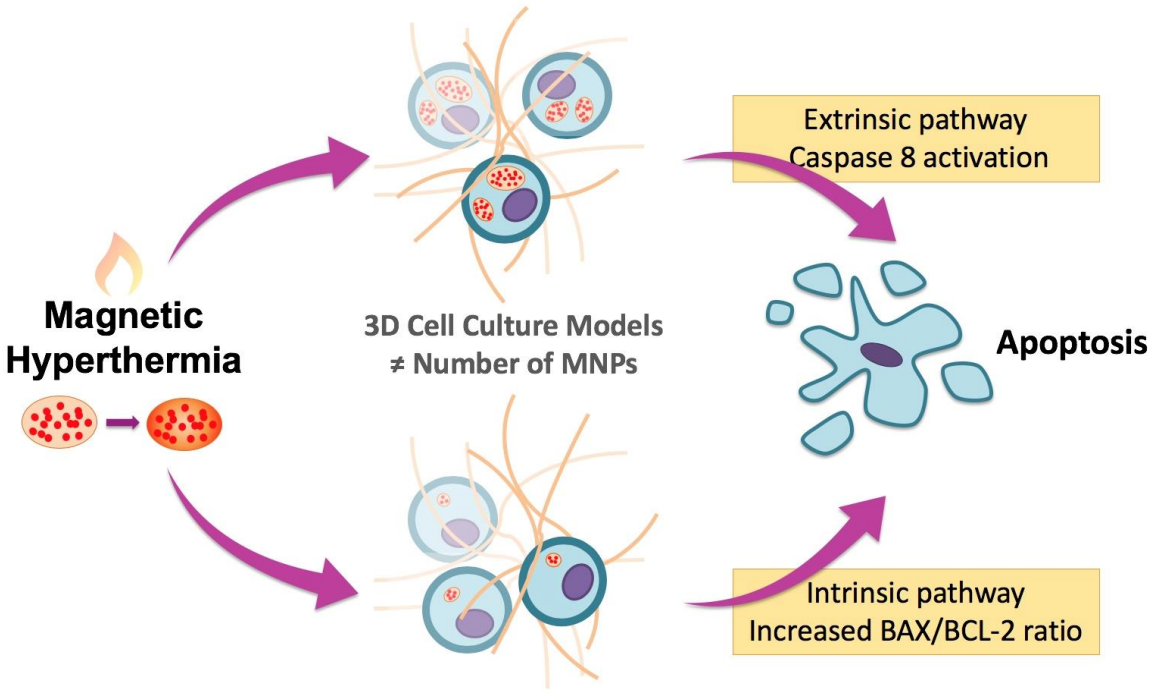

Keywords: iron oxides, nanoparticles uptake, magnetic hyperthermia, apoptosis, cell death pathways, 3D cell culture, macrophages

Abstract

Magnetic hyperthermia is a cancer treatment based on the exposure of magnetic nanoparticles to an alternating magnetic field in order to generate local heat. In this work, 3D cell culture models were prepared to observe the effect that a different number of internalized particles had on the mechanisms of cell death triggered upon the magnetic hyperthermia treatment. Macrophages were selected by their high capacity to uptake nanoparticles. Intracellular nanoparticle concentrations up to 7.5 pg Fe/cell were measured both by elemental analysis and magnetic characterization techniques. Cell viability after the magnetic hyperthermia treatment was decreased to < 25% for intracellular iron contents above 1 pg per cell. Theoretical calculations of the intracellular thermal effects that occurred during the alternating magnetic field application indicated a very low increase of the global cell temperature. Different apoptotic routes were triggered depending on the number of internalized particles. At low intracellular magnetic nanoparticle amounts (below 1 pg Fe/cell), the intrinsic route was the main mechanism to induce apoptosis, as observed by the high *Bax/Bcl-2* mRNA ratio and low caspase-8 activity. In contrast, at higher concentrations of internalized magnetic nanoparticles (1 – 7.5 pg Fe/cell), the extrinsic route was observed through the increased activity of caspase-8. Nevertheless, both mechanisms may coexist at intermediate iron concentrations. Knowledge on the different mechanisms of cell death triggered after the magnetic hyperthermia treatment is fundamental to understand the biological events activated by this procedure and their role in its effectiveness.

Introduction

Magnetic hyperthermia (MH) has been proposed as a promising strategy for cancer treatment.[1] Iron oxide nanoparticles are the most commonly used material for this purpose, given their biocompatibility associated to their physical and chemical properties.[2] Upon exposure to an external alternating magnetic field (AMF), the magnetic nanoparticles (MNPs) release heat to the surrounding environment, likely causing a local temperature increase around them.[3-4] It must be pointed out that still there is a debate on the very essence of this local temperature increase, as it cannot be explained by current theories.[5] This treatment is able to trigger cell death. Nevertheless, there is still a lack of control on the cell death mechanisms that are induced during the treatment.

It is fundamental to understand the type of cell death mechanism triggered by the MH treatment, as it might induce distinct cancer cell responses. When analyzing the effect of the global temperature increase in the mechanisms of cell death, it has been previously described that at high temperatures (above 55 ºC) necrosis - an accidental cell death (ACD) - is the main cell death pathway, causing a structural dismantling of the cells and releasing their intracellular content in an uncontrolled manner. In such case, the lack of molecular activation of specific molecular pathways could result in undesired inflammatory and cytotoxic responses.[6] In contrast, when reaching lower global temperatures (42-47 ºC), regulated cell death (RCD) mechanisms are the main mechanisms that are triggered by the molecular machinery leading to a preservation of the plasma membrane integrity and, therefore, not inducing inflammatory response.[6-11] Mixed events - RCD and ACD - could also be occurring in cell populations depending on the thermal stimuli used. Therefore, a careful control of the temperature should be achieved during hyperthermia treatments in order to prevent ACD and promote RCD.

In the particular case of using nanomaterials to produce heat, as in the case of MH, the mechanisms involved in the cell death signaling have not completely been described yet. In general, it is accepted that most iron oxide nanoparticles are often internalized by the cells remaining in intracellular vesicles, such as endosomes or lysosomes, depending on the time since the internalization.[12-15] Then, upon exposure to the AMF, hot spots can be produced inside the cell, leading to non-homogeneous temperature profiles. In fact, it has been previously described that during the magnetic hyperthermia treatment a local temperature increase is observed near the particles, while no global temperature increase occurs.[16-18] If the particles are located inside lysosomes, the energy they release may cause lysosomal membrane permeabilization (LMP).[19-20] As a consequence, the release of the lysosome proteolytic content to the cytosol occurs, inducing cell death that could even cause a bystander effect impacting surrounding cells. [21-24] Such cell death may occur by different routes (included in both RCD and ACD categories) depending, for example, on the magnitude of the membrane permeabilization.

The possibility of modulating the different cell death pathways would allow to control their associated biological consequences. For instance, the immune system activation might be different. Immunogenic cell death (ICD), described initially as an exclusive cell death mechanism to protect the body against pathogens, is nowadays known as a cell defense mechanism in the absence of pathogens. In fact, apart from necrosis that has been classically considered as immunogenic, other types of cell death such as regulated necrosis [25] and apoptosis [26-28] trigger also immune response because of the generation of danger-associated molecular patterns (DAMPs). It has also been demonstrated that caspases involved in the intrinsic apoptosis pathway offer an immunosuppressing effect, silencing the immune response of this pathway.[29-30] Cell death mechanisms are not exclusive, and it seems reasonable to consider that a specific stimulus could

trigger a mixture of unpredictable events. All this recent knowledge makes it very interesting to try to elucidate the death routes triggered under different conditions of MH treatment, because of the biological implications, like immunogenicity and final effectiveness of the treatment.

In a previous work we observed the effect of the MNP concentration on the cell death mechanisms after the MH treatment.[9] In cells with the highest amount of MNPs, necrosis was observed 24 h after exposure to the AMF. In contrast, when a lower amount of MNPs was localized inside the cells, cell death was mainly induced by apoptosis. Other studies also described the cell death mechanisms associated with heat production during the magnetic hyperthermia treatment.[8, 31-32] However, in all these studies, little has been evaluated about the influence of MNP concentration on the molecular mechanisms that determine the different apoptotic pathways triggered during the treatment.

In the present work, we used a 3D cell culture model previously reported,[9] as this kind of model mimics in a more realistic way the cellular environment in the tumor than 2D cell cultures.[33-34] A highly phagocytic macrophages cell line (RAW 264.7)[35] was used and cells were challenged with different amounts of MNPs. MNP uptake was evaluated by flow cytometry (FC), confocal microscopy, Inductively Coupled Plasma Optical Emission Spectrometry (ICP-OES) and magnetometry. Apoptosis induction 24 h after the exposure to AMF was also evaluated by flow cytometry. Computational analysis was used to evaluate the MNP heating performance after cell internalization. In addition, after the MH treatment, *Bcl-2*, *Bax* and *Bid* gene expression as well as caspase-8 activity were determined through Reverse Transcriptase quantitative polymerase-chain-reaction (RT-qPCR) and a protein colorimetric assay, respectively. This approach was designed to elucidate the molecular mechanisms of apoptosis induced by the MH treatment as a function of the number of internalized particles. The possibility of controlling the activation of

such mechanisms could be the basis to establish the optimal conditions of the MH treatment and to predict the future efficacy of the therapy.

Results & Discussion

Preparation and characterization of MNPs

The synthesis and functionalization of 11 nm superparamagnetic iron oxide MNPs coated with PMAO (poly(maleic anhydride-alt-1-octadecene) and functionalized with glucose (Glc) was discussed in a previous published work.[9] Their core size (Fig. 1), low polydispersity, magnetic properties and low cytotoxicity,[9] previously demonstrated their suitability for *in vitro* MH studies and, therefore, we chose the same material for the present work. The polymeric coating with PMAO allowed the transference of the MNPs from organic solvents used during the synthesis to aqueous medium. In this study, PMAO was modified with the fluorophore TAMRA (carboxytetramethylrhodamine), to be used for FC and confocal microscopy studies.[29] The glucose functionalization prevented nanoparticle aggregation in cell culture medium supplemented with Fetal Bovine Serum (FBS) and promoted nanoparticle internalization in cells (Supporting Information, Fig. S1).[29] This functionalization was also chosen as it promotes endocytosis and results in an intracellular localization in lysosomes.[29]

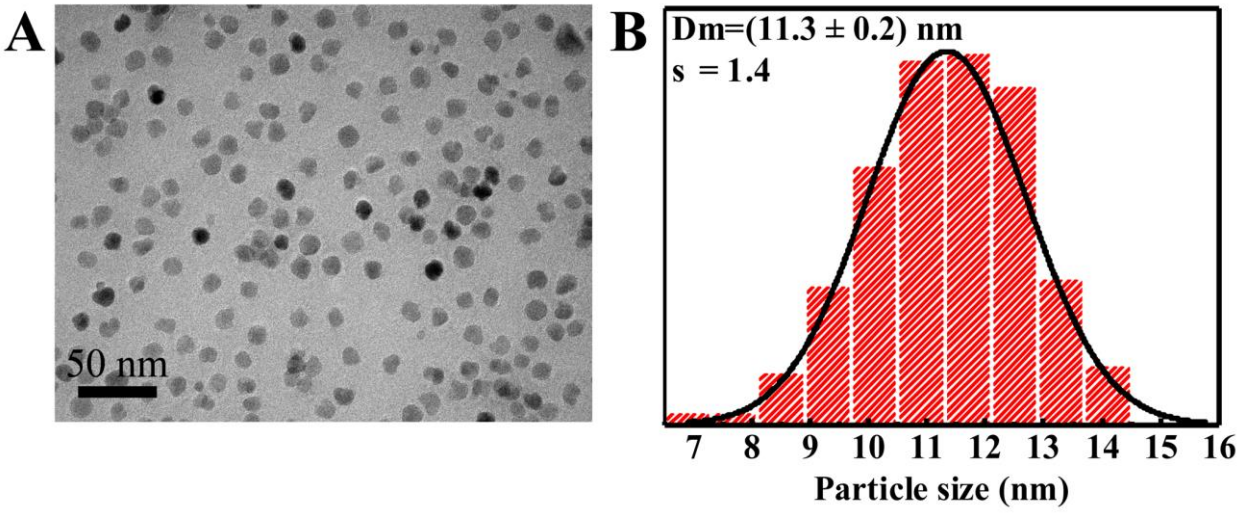

Figure 1. (A) TEM image of the MNPs. (B) Particle size distribution analysis.

The efficacy of the polymer coating (PMAO modified with TAMRA), as well as the glucose functionalization was verified by analysis of electrophoretic mobility (Rf) and ζ potential. The MNP characterization evidenced a decrease on the MNP negative charge from -22.0 ± 0.1 mV, before functionalization, to -9.0 ± 0.6 mV after glucose addition. In agreement with these changes, a decrease in MNP mobility during electrophoresis was observed after the glucose functionalization, in agreement with previously reported functionalization (Supporting Information, Fig. S1). The hydrodynamic size of the Glc-functionalized particles suspended in PBS at pH = 7 was 85 ± 7 nm.

The specific absorption rate (SAR) was also evaluated before the *in vitro* MNP studies to determine the heating efficiency in suspension. The SAR value was 104 W/g Fe ([Fe] = 1 mg/mL, H= 20 kA/m, f= 829 kHz). Although the SAR measurement of the MNPs suspension may not be representative of the physical behavior of the MNPs once internalized in the cells, when combined with theoretical analysis it allows estimation of the MNPs heating capacity in the conditions used for the *in vitro* experiments, as will be described below.

Validation of a panel of 3D cell culture models with different amounts of MNPs per cell

As mentioned earlier, one of our main objectives was to evaluate the effect of different amounts of MNPs internalized by the cells on the efficacy of MH treatment and the pathways triggered towards cell death. For that purpose, the generation of a reproducible 3D cell culture model was a better option to mimic the *in vivo* environment compared to the classical 2D cell culture models.[33, 36-38] Our 3D model was based on a highly phagocytic cell type, such as macrophages (RAW 264.7)

that present a high capacity to phagocyte the MNPs due to their biological functions.[39-40] Our previous results with this cell line had already pointed to the important effect that the number of internalized particles had on the cell death mechanism triggered.[9] Collagen, which is a major component of the extracellular matrix in the tumor tissue, was selected to generate the 3D matrix. The use of collagen provided a very easy system to release the cells from the 3D culture for a posteriori analysis, through a fast, simple and low cytotoxic enzymatic procedure.[9]

Our approach was based on the preparation of 3D cell culture models containing different amounts of particles per cell, named M1, M10, M25, M50, M75 and M100 depending on the iron amount used to treat the cells before they were entrapped within the collagen matrix. To achieve this, cells in suspension (0.5 mL) were first incubated with different MNP amounts for 1 h (Total amount of iron = 1, 10, 25, 50, 75 and 100 μg). Then, cells were washed to remove all the non-internalized MNPs.

The nanoparticle uptake by the cells was evaluated and quantified through ICP-OES, magnetic measurements and FC. ICP-OES measurements showed that increasing amounts of total intracellular iron were obtained when increasing the amount of MNPs used during the incubation step (Fig. 2A, Table 1). The highest intracellular iron amount achieved was 7.5 pg Fe/cell, which is in good agreement with data published about MNPs internalized in similar phagocytic cell lines.[10] In addition, the intracellular iron content was also determined through AC magnetic susceptibility measurements and subsequent data analysis (Fig. 2B). This technique, contrary to ICP-OES measurements, allowed quantifying the iron forming part of the MNPs, as it can be distinguished from other naturally occurring iron-containing species.[41] In order to do that, the height of the signal of the out-of-phase susceptibility corresponding to the relaxation phenomenon of the particles was compared to that of the original particles. The iron amount per cell calculated

by both methods (ICP-OES and AC magnetic susceptibility analysis) was very similar (Fig. 2A), indicating that most of the intracellular iron was in the form of MNPs. These results allowed calculating the internalized number of particles, N, for each preparation (Table 1). Interestingly, the detection limit of the magnetic quantification was lower than that of the ICP-OES, allowing to measure ≈ 0.1 pg of iron (in the form of MNPs) per cell for the lowest amount of iron used during the incubation step (Fig. 2A).

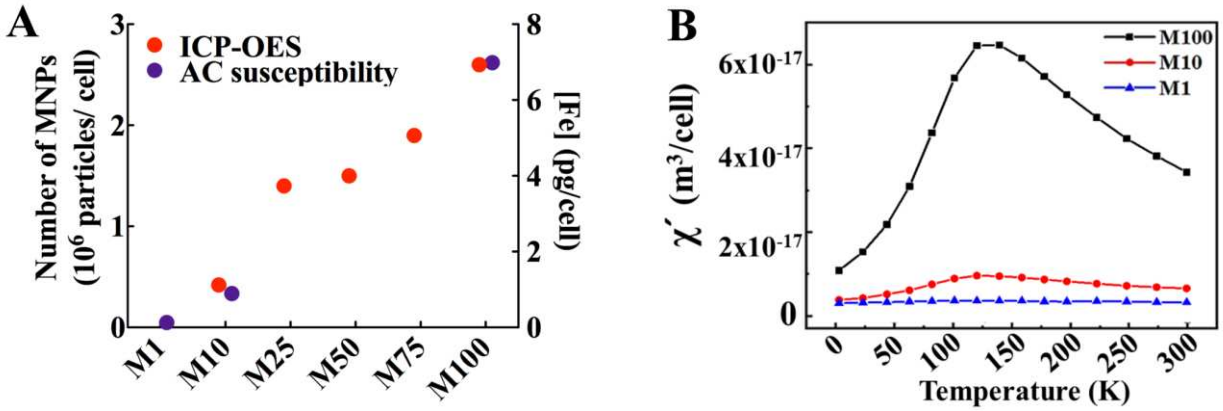

Figure 2. (A) Number of internalized particles and the corresponding iron concentration per cell determined by ICP-OES and magnetic measurements. (B) Temperature dependence of the in-phase component of the AC magnetic susceptibility of cell samples.

These two techniques (ICP-OES and magnetometry) provided average data per cell, assuming that the distribution of MNPs was homogeneous among all cells. As such, we further evaluated the particle distribution by fluorescence microscopy and flow cytometry.

Flow cytometry analysis, of cells released from the 3D cell cultures, showed that almost all the cells incubated with the highest amounts of MNPs had internalized MNPs (about 94 % of the total number of cells in models M50, M75 and M100) (Fig. 3, Table 1). Decreasing the amount of MNPs during incubation resulted in a lower percentage of cells containing MNPs. In particular, in M25

and M10 models the percentage of cells containing MNPs decreased to 86 % and 57 %, respectively. Furthermore, in M1 only 6% of the cells had incorporated MNPs (Fig. 3A).

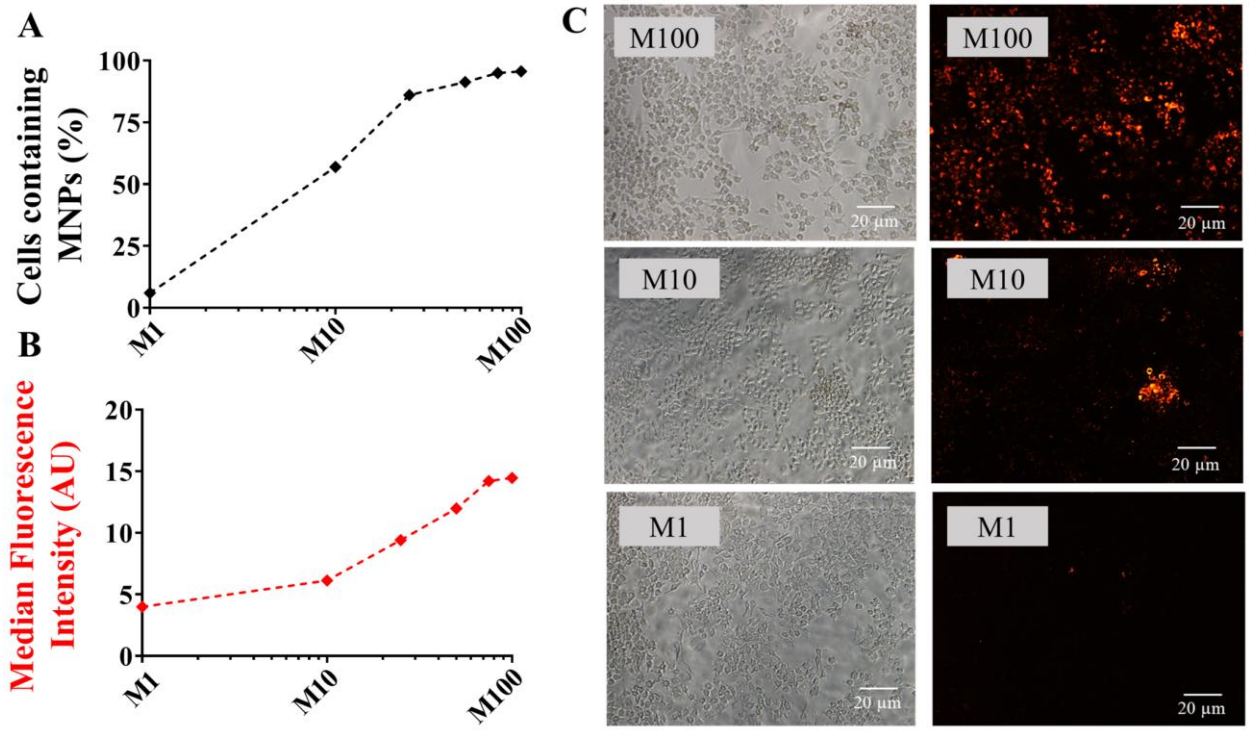

Figure 3. (A) Percentage of MNP-loaded cells and (B) Median Fluorescence Intensity values of the cells released from the different 3D models. Data obtained from flow cytometry analysis. (C) Bright field (left) and fluorescent red channel (right) images of cells from M1, M10 and M100 models. Scale bar: 20 µm.

The median fluorescence intensity (MFI) data showed that, although the percentage of cells containing MNPs was similar at the highest concentrations, their corresponding MFI kept increasing as a function of the amount of MNPs during incubation (MFI_{M50}=11.9; MFI_{M75}=14.2; MFI_{M100}=14.5) (Fig. 3B). These data indicated that a higher amount of MNPs were internalized per cell for increasing iron concentrations, in agreement with the quantification assays performed.

These results further agreed with the fluorescence and optical microscopy images (Fig. 3C). Images showed that for the system with the highest number of internalized particles (cells for M100), all cells contained large aggregates of particles, associated to the entrapment of the MNPs inside intracellular vesicles, probably lysosomes, as previously demonstrated by our group using similar particles with the same coating, functionalization and incubation times using 2D cell cultures.[29] The images from the cells used to prepare model M10 showed, in general, a lower fluorescence signal from the MNPs per cell. In addition, cells with no apparent signal from the particles (or at least under the detection limits of the technique) were also observed. With this technique, it was also possible to determine that the intracellular distribution of the MNPs was not homogeneous as some cells contained large aggregates of particles.

Taken together, the ICP-OES, the magnetic characterization, the FC and the microscopy supported the achievement of cell samples with different internalized number of particles that allowed the preparation of 3D cell culture models with varying amounts of MNPs per cell. Nevertheless, it should be considered that for the system with the lowest number of internalized particles, a significant number of cells did not contain any particles.

Table 1. Summarized values related to the magnetic nanoparticles uptake by cells used to prepare the different 3D models. The percentage of MNP-loaded cells has been calculated from flow cytometry data. The amount of internalized iron and the corresponding number of particles per cell have been calculated from the ICP-OES measurements.

Model	Fe amount administered (μg)	MNP-loaded cells (%)	[Fe] $_{internalized}$ (pg/cell)	Number of particles per cell
M100	100	95.6	7.5	2.6×10^6
M75	75	94.9	5.4	1.9×10^6
M50	50	91.3	4.4	1.5×10^6
M25	25	86.1	3.9	1.4×10^6
M10	10	57.0	1.2	4.2×10^5
M1	1	6.0	<MCD	<MCD

In summary, these results confirmed a correlation between the MNP amount administered during the incubation time and the number of MNPs taken up by cells, although the resulting intracellular distribution was not homogeneous. Despite some limitations, we had the capability to control the number of particles inside the cells, a key development to study the effect of the magnetic hyperthermia treatment on cell death as a function of the intracellular heat production. After verifying that different amounts of MNPs were internalized by the cells, the 3D cell cultures were generated by mixing collagen with the cells containing the MNPs.

Effect of the magnetic hyperthermia treatment on the cell death

Cell viability was evaluated 24 h after the exposure of the 3D cell cultures (M1 to M100), to mild hyperthermia conditions (H= 13 kA/m; *f*= 377 kHz; t= 30 min) (Fig. 4A). As control, cell viability was also assessed in cells not exposed to MNPs or AMF, in cells only exposed to AMF and in M100 cells without AMF (Fig. S2). Cell viability after AMF treatment decreased drastically

with increasing amounts of internalized MNPs (Fig. 4A). The combination of AMF treatment with the highest amounts of MNPs (M75 and M100) led to a high reduction of cell viability (down to 9 ± 4 % of viable cells for both models). It should be noted that for both controls (M100 cells not exposed to AMF or cells only exposed to AMF) a small reduction of cell viability was observed (≈ 80 % viable cells, Fig. S2), indicating that the high reduction observed for M100 is due to the combination of both treatments, MNPs and AMF. Exposure of M10, M25 and M50 models to AMF induced also a significant loss of cell viability (23 ± 5, 20 ± 2 and 16 ± 2 % of viable cells respectively, Fig. 4A). Finally, in model M1, a less severe effect was observed (65 ± 7 % of viable cells). In order to further understand the mechanism underlying the loss of cell viability induced by the combination of AMF and MNPs, different apoptotic markers were evaluated.

The number of viable, apoptotic (early and late) and necrotic cells was monitored by FC using two fluorescent markers: Annexin V (a cellular protein that binds to phosphatidylserine (PS)) modified with FITC (Fluorescein isothiocyanate) and propidium iodide (PI).[42] The loss of cellular membrane asymmetry is an early event in the apoptotic process and can be measured through the detection of PS residues on the outer side of the membrane, marked with Annexin V. The paired labelling with PI, a DNA intercalator agent which is not able to penetrate intact membranes, was used to detect the plasma membrane disruption typical of late apoptotic / necrotic events.

The FC analysis demonstrated a strong correlation between the amount of intracellular MNPs and the response to AMF (Figs. 4 and S2). A general trend was observed when analyzing the percentages of both early apoptotic (AnnV+PI-) and late apoptotic (AnnV+PI+) cells after AMF (Fig 4B). An increase in the percentage of AnnV+ cells was observed with the increase of internalized MNPs (Fig. 4B). The increase of AnnV+PI+ cells was particularly high for the M50, M75 and M100 models, with 7, 9 and 15% of cells in the late apoptotic state respectively (Fig.

4B). Interestingly, almost no viable cells were observed when cells were incubated with the highest amount of MNPs (M100) and exposed to AMF (Fig. 4B). Once again in M100 cells in the absence of AMF we observed a high percentage of viable cells (Figs. 4C and S2) indicating that the loss of viability and apoptosis induction was due to the treatment combination. Additionally, for all the tested conditions almost no cells in necrosis were observed (Figs. 4 and S2).

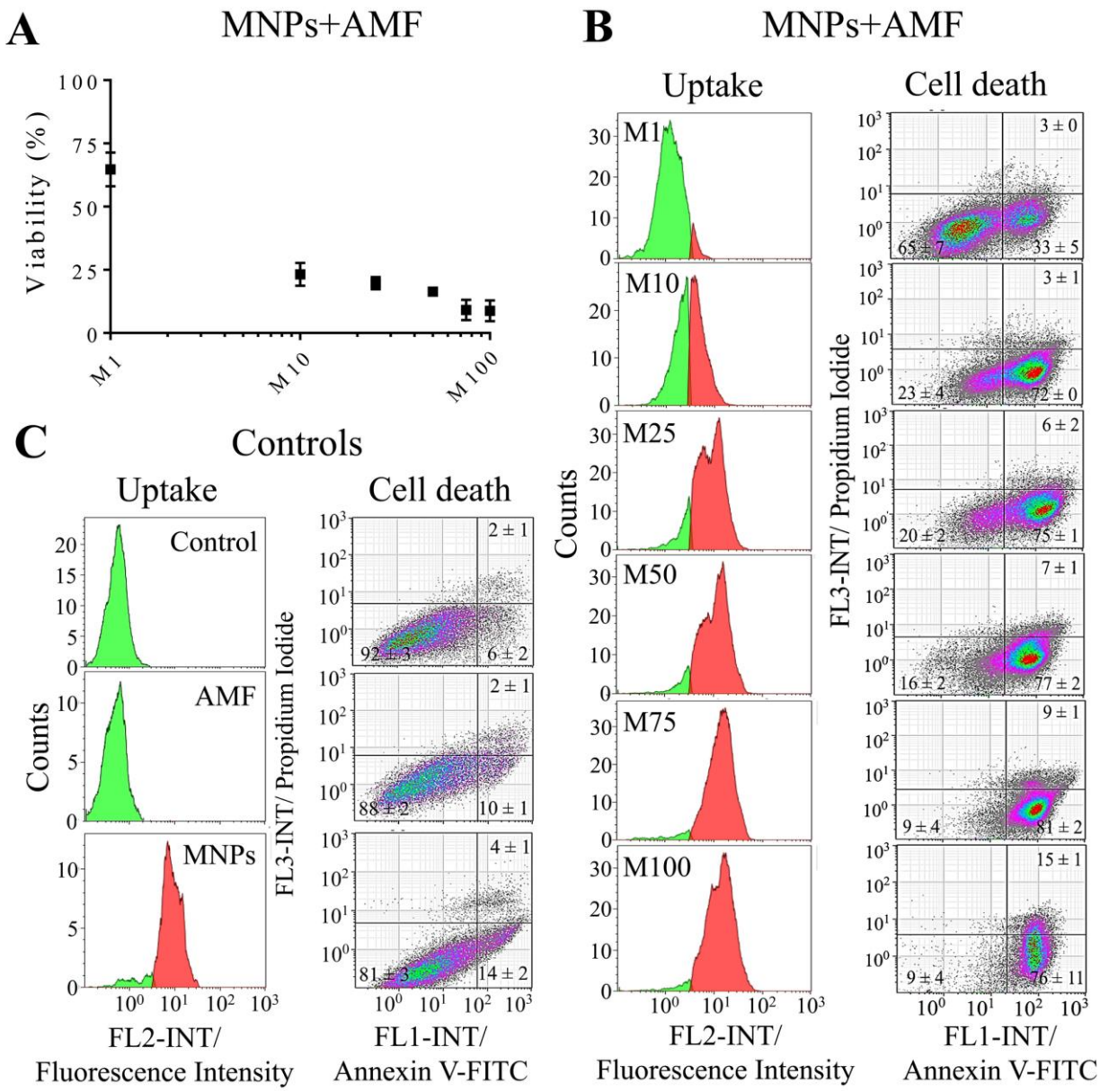

Figure 4. Flow cytometry analysis of nanoparticles uptake and cell death. (A) Viability analysis for all the samples containing MNPs and exposed to the AMF (See Supporting Information for the analysis of the control samples, Fig. S2), (B) Cells from different models containing MNPs treated with MH (M1 to M100), (C) Control samples, including untreated cells, cells exposed to the AMF and cells incubated with the highest amount of MNPs (same amount as M100) but not exposed to the AMF.

Taken together, these results indicated a correlation between the number of internalized particles and the corresponding cell response as a consequence of the alternating magnetic field exposure, triggering in all cases apoptosis. As no overall temperature increment (ΔT) of the cell culture media was observed during the MH experiment, localized thermal effects appeared as a possible cause of the biological effects being triggered and were subsequently evaluated.

Local thermal effects occur during the AMF exposure

As mentioned before, reaching different global temperatures in the cell culture media have been associated with different cell death mechanisms.[6, 43] However, it has been previously observed that, counterintuitively, MH experiments leading to cellular death do not necessarily lead to a global temperature increase.[16-17, 20] Little is known about the biological responses triggered by a temperature increase locally inside the cells. It has been shown that nanoparticles could produce a significant temperature increase near their surface,[11] but little has been evaluated about the impact on the heat produced in such hot spots on the whole cell temperature.[17, 19-20] Measuring temperature with the required resolution to evaluate these processes still remains a very complicated task.

In order to provide an understanding of the local thermal effects occurring within the cells during the AMF exposure a theoretical simulation was performed (Fig. 5), particularly focusing on elucidating the feasible heating performance when the particles are internalized by the cells, under different interparticle interactions and field conditions. In addition, a simple estimation of the temperature increase within the vesicles containing the particles and the entire cell was made as a function of the internalized number of particles. For these simulations experimental data regarding the amount of internalized MNPs (obtained from the ICP-OES and magnetic susceptibility measurements) and their internalization pattern within vesicles of different sizes (obtained from confocal microscopy images) were used.

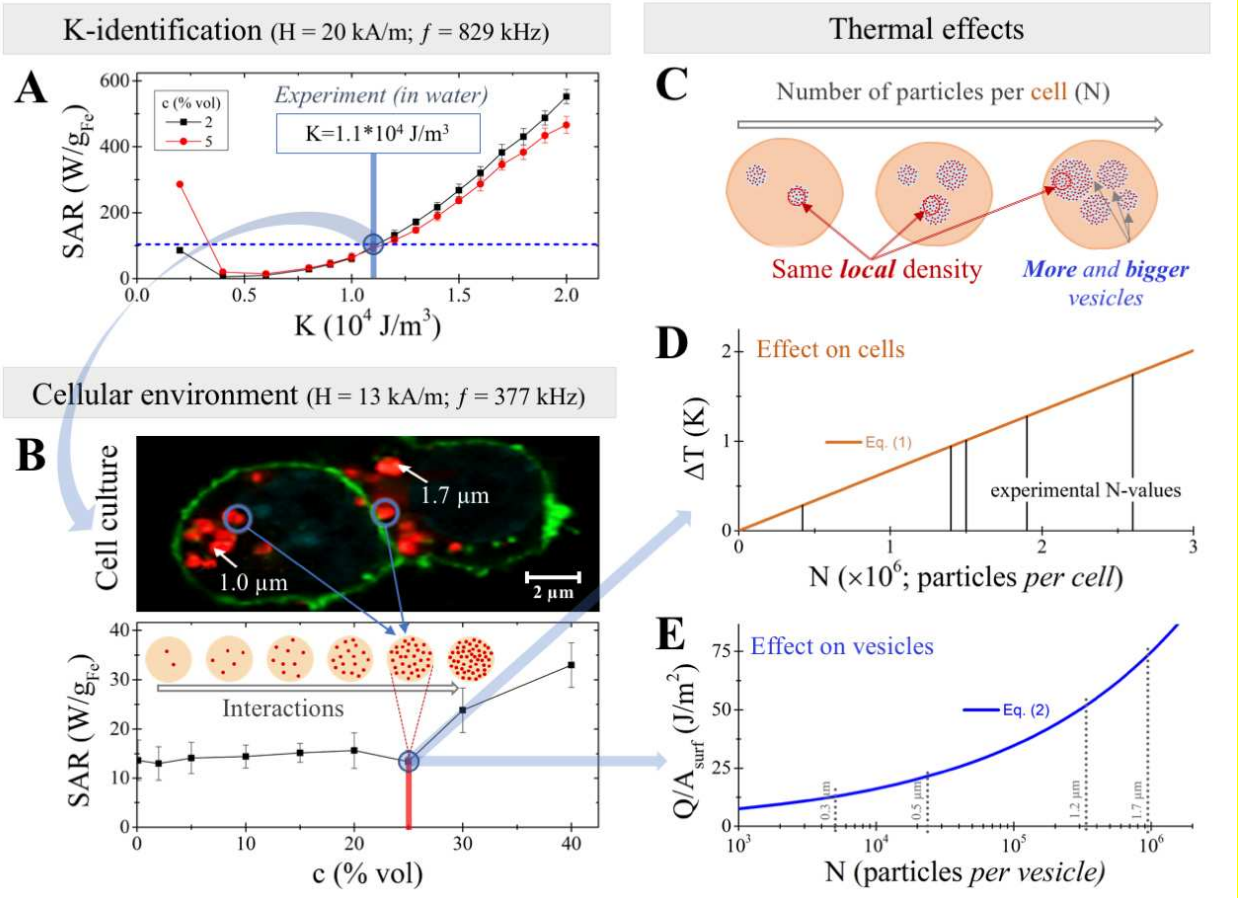

Figure 5. Computational analysis of the thermal effects. (A) Identification of the anisotropy constant of the particles, K, through the comparison of computationally predicted SAR and the experimental value measured in water (K-identification). (B) Estimation of the SAR performance of the particles occurring during the *in vitro* conditions, using the previously identified K value (Cellular environment). (C) Schematic representation of the number and size of vesicles in the different models depending on the number of internalized particles per cell. (D) Estimation of the dependence on number of particles (N) of ΔT of the whole cell with the obtained SAR for the cellular environment; the vertical solid lines correspond to the experimental cases. (E) Estimation of the dependence on number of particles (N) of flow of energy density through the vesicles containing MNPs' wall with the obtained SAR for the cellular environment; the vertical dotted lines indicate the corresponding average vesicle sizes.

Given that the field conditions and the interparticle interactions during the *in vitro* experiments were different than those used for SAR characterization in water suspensions, a previous step was necessary to estimate the heating power of the particles within the conditions of the *in vitro* experiments, especially, given the strong effect that interparticle interactions may have on the SAR values.[44-45] Firstly, the anisotropy constant of the particles (K), key parameter for heat generation, was identified (Fig. 5A).[46-48] To do so, the SAR measured for the particle suspension (MNPs occupying about 2% of the volume, H= 20 kA/m, *f*= 829 kHz) was simulated using a computational kinetic Monte Carlo technique and considering K as a free parameter (see Supporting Information - section "computational details" including Figures S3 and S4 for more information).[49] The K value was identified as the one at which experimental and simulated SAR values matched, resulting in $K=1.1*10^4$ J/m^3, in reasonable agreement with related studies.[50-51]

Results illustrated the complex role of interactions, which can either decrease or increase the SAR depending on K (Fig. 5A) for 2% and 5% of occupied volume fraction.[47]

Secondly, this K was used to simulate the SAR of the particles when internalized by the cells, where the particles were closely packed within vesicles, probably lysosomes. The SAR corresponding to the *in vitro* conditions (H= 13 kA/m, *f*= 377 kHz) was calculated assuming a packing fraction of magnetic material of about 25%, that was obtained considering the particle iron oxide core size and a 2 nm coating associated to the PMAO linked to the iron oxide surface (Fig. 5B).[3] Note that the large number of particles per vesicle (thousands) allowed discarding finite-size clustering effects. The SAR value obtained in such conditions was ≈ 14 W/g Fe, significantly lower than the one measured experimentally for the water suspension. This reduction in the SAR values would be a consequence of the different AC field measuring conditions and the different local particle concentration. In fact other studies had previously indicated the large reduction of the SAR values once the particles were internalized by the cells.[15, 52-55] Nevertheless, as observed in the previous section (Fig. 4), this heating capacity was still able to induce cell death.

The SAR value obtained for the *in vitro* conditions was then used to estimate the increase in temperature both in the vesicles and in the whole cell. For the analysis of ΔT inside the vesicles, a quick estimate in the spirit of Andra et al.[56] indicated a negligible temperature rise of the vesicle (from ~10^{-6} at its centre, to ~10^{-5} K at the surface), suggesting the rise of temperature per se not to be the origin of the different cellular results observed. Thus, we focused on the analysis of ΔT within the whole cell, considering that the heat was released from the vesicles to the entire cell. Assuming that the heat flowed from within the vesicles to the surrounding cell but that flow outside the cell was negligible (based on the observed global ΔT ≈ 0 K), ΔT as a function of N was naïvely estimated as (see Supporting Information for details)

$$\Delta T_{cell} = \frac{SAR \cdot \Delta t \cdot N \cdot \rho_{MNP} \cdot d^3}{c_{H_2O} \cdot \rho_{H_2O} \cdot d_{cell}^3} \quad (1),$$

where SAR was the value obtained from Figure 5B; Δt is the time variation during the assumed adiabatic behavior; ρ_{MNP} (c_{MNP}) and ρ_{H2O} (ρ_{H2O}) is the density (specific heat capacity) of the magnetic nanoparticles and water, respectively (note that the heat capacity of the cell is assumed to be the same as that of water); *d* is the particle diameter and d_{cell} stands for the average cell size. Using Eq. (1) with Δt = 20 s (based on our own experimental observations of ΔT *vs*. Δt linearity), for the experimental conditions it was obtained an essentially linear behavior (Figure 5D). The relatively small absolute values predicted were concordant with the observed global ΔT ≈ 0 K and the intuitive idea of higher heating with larger number of internalized MNPs. It is interesting to note that a more realistic estimate considering heat flow outside the cells would result in negligible ΔT (again of the order of ~10^{-5} K).[56]

Assumptions made for Eq. (1) make it only valid for a small initial time interval, limiting its capability to grasp the long-timescale experimental dynamics. A complementary approach to obtain further information is to consider the corresponding rate of heat flow (ΔQ) through the vesicle wall. The areal density of heat flow through the vesicle membrane, which depends on the vesicle size was estimated as (see Supporting Information for details)

$$\frac{\Delta Q}{S_{ly}} = \frac{1}{6} SAR \cdot \Delta t \cdot N^{\frac{1}{3}} \cdot \rho_{MNP} \cdot d \cdot c^{\frac{2}{3}}, \quad (2)$$

where c is the volume fraction (0.25) and S_{ly} is the surface area of the vesicles. The results as a function of N (Fig. 5E), indicated a non-linear growth of ΔQ with particle number; note that in this case N is directly proportional to vesicle size, as the packing fraction is constant. For bigger vesicles a much larger heat flux per surface area was predicted in comparison with the values obtained for smaller vesicles. In our models, both the number and size of the vesicles increased significantly with the number of internalized particles, reaching diameters up to 1.7 μm for model

M100 while for model M10 lysosome diameters only reached 1 μm. These differences may play a very important role in the way the heat is transmitted to the rest of the cell, suggesting that further investigations should be performed to elucidate the real influence that the vesicle size has in the thermal effects occurring during the AMF exposure. The question to elucidate is whether different rates of heat flow might produce different effects on the cellular membrane, in particular more damage due to increased heat flux.

Taken together, all these results indicated that in our cell models, even in the ones with the lowest amount of internalized MNPs, a localized effect (at the level of the organelles containing the particles) may have occurred and be responsible for the different responses observed. Our results allowed speculation that the effect may be related to the different rates of heat flow through the vesicle wall, but certainly further work is needed to explore this possibility. Following this idea, the vesicle size was identified as a fundamental parameter in the heat flux between these organelles and the cells. It can be envisaged that vesicles containing the MNPs, probably lysosomes, are key organelles to control the biological response to the heat produced during the MH treatment. As previously described by other authors, the energy released from the particles located inside lysosomes may cause lysosomal membrane permeabilization during the MH treatment, subsequently inducing cell death.[19-20] Our results suggested the possible fundamental role of the size of these organelles on the biological response to the thermal stimuli. This parameter would be an important aspect to assess when analyzing the internalization of MNPs in different cancer cell lines in MH related studies.

The number of intracellular MNPs affects the activation of different cell death pathways

So far, our results suggested that the MH treatment induced a clear apoptotic response with different rates depending on the amount of internalized MNPs (Fig. 4) and that according to the model calculations different thermal effects could be occurring with higher and lower number of internalized particles (Fig. 5). The analysis of the ratio of cells in early and late apoptotic stages indicated, as expected, that higher intracellular amount of MNPs produced a more intense and faster apoptotic cell death (Fig. 4). However, Annexin V-FITC/PI FC assay by itself did not provide any additional information concerning the type of apoptotic pathway triggered in the presence of the different amounts of MNPs and hyperthermia.

At the molecular level, apoptosis is characterized by the activation of caspases (cysteinyl, aspartate specific proteases) (Scheme 1). There are two main pathways for activation of apoptosis depending on the stimuli: through external death receptors (an extrinsic pathway) or through internal signals linked to the mitochondria (intrinsic pathway).[57] Activation of the extrinsic cell death pathway occurs by the binding on the cell surface of specific ligands (e.g. TNF-related apoptosis-inducing ligand, TRAIL), coming from the environment or neighboring cells,[28] to death receptors. This binding induces activation of pro-caspases (8 and / or 10) that are the initiators of apoptosis through the extrinsic pathway.[58-59] The intrinsic route is activated by intracellular danger signals and controlled by the BCL2 protein family through mitochondrial permeabilization. This route can be activated by numerous intracellular death signals, such as DNA damage, oncogene activation, growth factor deprivation or microtubule disruption.[31, 59] Both pathways are also connected. In some types of cells, the extrinsic pathway is often not enough to produce cell death and requires an amplification via the intrinsic pathway.[57] In such cases, signaling starting through the death receptors (extrinsic pathway) may also lead to apoptosis *via* the intrinsic pathway through the activation of the BID/tBID proteins (also part of the BCL2 family).

It has been previously described that in Magnetic Intra-Lysosomal Hyperthermia (MILH) the heat produced by the particles located inside the lysosomes causes lysosomal membrane permeabilization (LMP) [44, 48, 50] resulting in the leakage of lysosomal enzymes into the cytosol.[60]. The molecular mechanisms of cell death induced upon lysosomal membrane disruption are extensive and have not yet been completely understood. The different lysosomal cathepsins that release into the cytosol following of LMP can trigger different signaling pathways to promote both the intrinsic and extrinsic apoptosis pathways.[60] However, their mutual importance varies depending on the stimulus that triggers the total or partial permeabilization of the lysosomal membrane.[61]

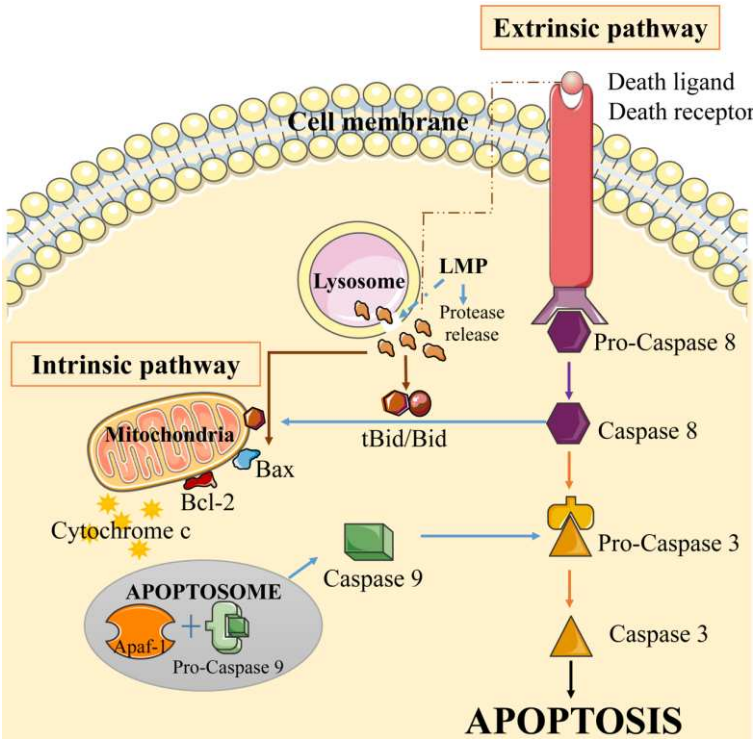

Scheme 1. Schematic representation of the molecular events triggered by both extrinsic and intrinsic apoptotic pathways.

To further clarify the apoptotic route triggered during the MH treatment, *Bax* and *Bcl-2* expression levels, associated with the intrinsic pathway, and caspase-8 activity, associated with the extrinsic pathway, were assessed in 3D cell culture models exposed to the AMF and to the different amounts of MNPs. In addition, *Bid* expression was also monitored to evaluate the crosstalk between the extrinsic and the intrinsic pathways that would allow the initiation through the extrinsic pathway and finalization through the intrinsic pathway.

First, we studied the impact of the internalization of MNPs on the *Bax* and *Bcl-2 mRNA* levels in cells not exposed to the AMF (Fig. 6A). Our results showed that there were no significant differences in the expression levels of *Bax* (pro-apoptotic) in the samples incubated with different amounts of MNPs. In contrast, an important overexpression was observed in the *Bcl-2* (anti-apoptotic) levels, that increased with increasing amounts of internalized MNPs until model M50, meaning that cells could counteract the presence of MNPs and did not need to trigger intrinsic apoptosis (Fig. 6A). In addition, to the independent measurements of the *Bax* and *Bcl-2* levels, calculating the ratio of these two proteins allowed evaluating the balance between pro and anti-apoptotic signals, providing information about the cell susceptibility to apoptosis and the apoptotic route being triggered.[62] Interestingly, at the two highest amounts of internalized MNPs (M75 and M100), there was a down-regulation of *Bcl-2* expression and a trigger of intrinsic apoptosis (increase of *Bax*/*Bcl-2* ratio up to values ≈ 2, between 10 and 100 times higher than for the rest of the models) (Fig .6A) This result was in line with the previous data indicating that, for the M100 cells, a more intense stress is observed triggering an apoptotic response (Fig. 4) with concomitant loss of cell viability (20%; Fig. 4A).

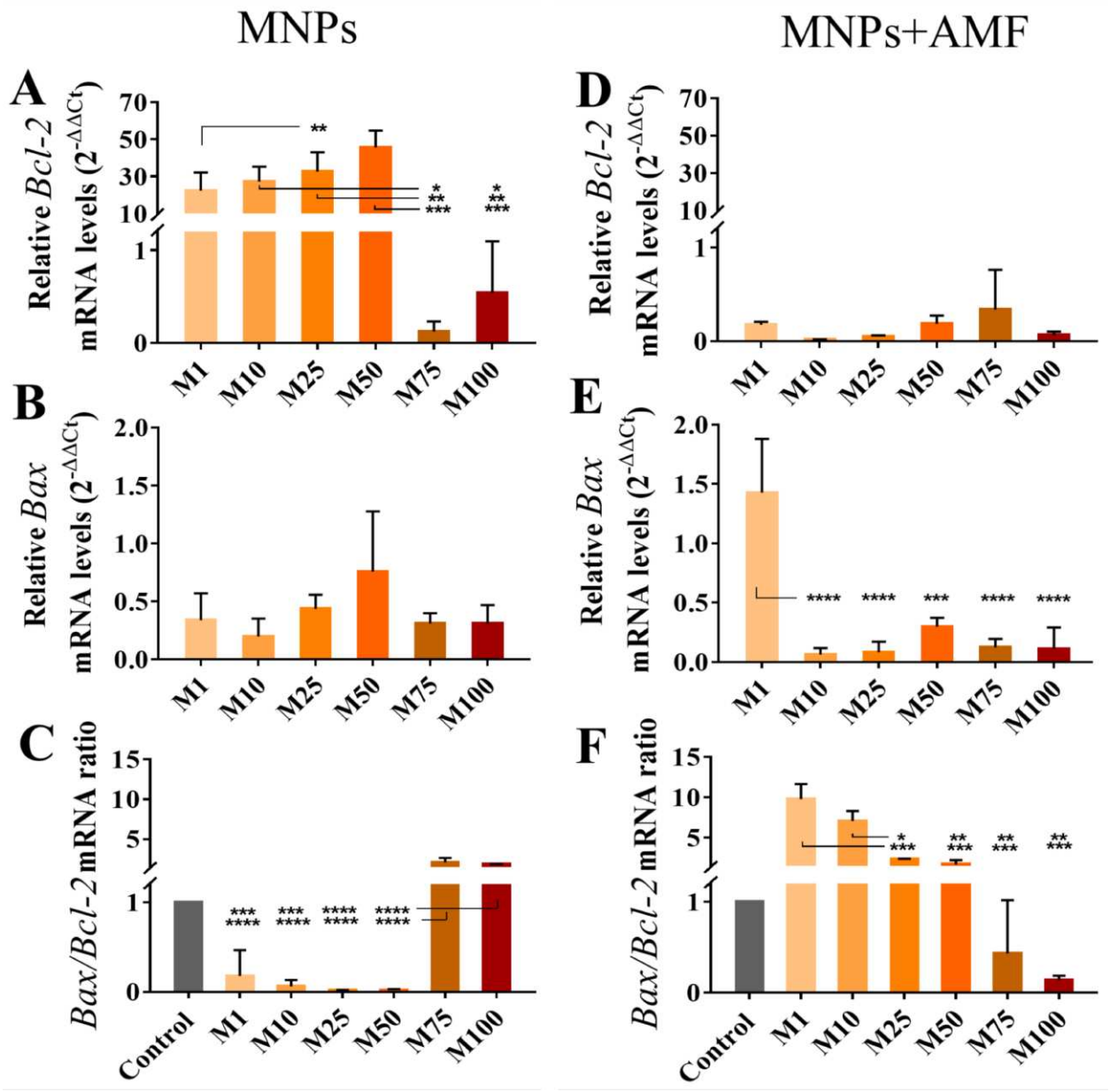

Figure 6. Analysis of the mRNA expression involved in the mitochondrial cell death apoptotic pathways of the different models studied before (A, B, C) and 24 h after (D, E, F) exposure to an AMF. Relative Bcl-2 (A and D) and Bax (B and E) mRNA levels were calculated normalizing each sample by the control cells´ value. In panels A, B and C, the control consisted of just cells, and in panels D, E and F the control consisted of cells without MNPs but exposed to AMF. Besides, Bax/Bcl-2 2 ratio (C and F) was calculated in order to compare the level of the intrinsic apoptotic

pathway with respect to the controls. Results show a clear upregulation of that pathway in the cells incubated with lower amounts of MNPs and exposed to the AMF. Statistical significance between the means was determined using a one-way ANOVA followed by Tukey's multiple comparisons test (****$p < 0.0001$; ***$p < 0.001$; **$p < 0.01$; *$p \leq 0.05$; $p > 0.05$ no significance).

We then analyzed the mRNA expression of these two genes in cells incubated with the MNPs and exposed to the AMF (Fig. 6B). For the model with the lowest MNP concentration, M1, a clear overexpression of the *Bax* mRNA levels was observed that, together with a decrease of the *Bcl-2* mRNA levels, resulted in a notable increase of the ratio *Bax*/*Bcl-2*, indicating that, under these conditions, the apoptosis was likely to take place through the intrinsic pathway. For the remaining MNP concentrations (M10 to M100), the mRNA levels of the anti-apoptotic gene *Bcl-2* remained stable and low and the mRNA levels of the pro-apoptotic gene *Bax* decrease compared to the level attained for M1, giving rise to a dose-dependent decrease of the *Bax*/*Bcl-2* ratio compared to the M1 sample. Values of *Bax*/*Bcl-2* ratio increased 7 and 10-fold for the M1 and M10, respectively and decreased down to 0.1 in the sample incubated with the maximum dose of MNPs, M100 (Fig. 6).

It is worth mentioning that the apoptotic population after MH treatment increased with the increase of MNP amounts. However, the implication of the intrinsic pathway seemed to decrease with increasing MNP amount. These results clearly indicated that the increase in the apoptotic cell death, up to certain concentration (M10), could be attributed mainly to the intrinsic pathway and justified by the increase of the observed *Bax*/*Bcl-2* ratio. However, for higher MNPs concentrations the increase in the apoptotic response did not fit with the levels of *Bax*/*Bcl-2* detected for these samples, indicating that other apoptotic routes might be playing a role. To evaluate this hypothesis,

the activation of the extrinsic pathway by MH treatment was assessed *via* caspase-8 activity, since caspase-8 is a key player in the activation of apoptosis through the extrinsic pathway. Four different samples were selected for this assay: a control without MNPs (AMF) and samples incubated with high (M100), intermediate (M10) and low (M1) amounts of MNPs and exposed to the AMF (MNP+AMF). The caspase activity was evaluated 24 h after the MH treatment. The analysis revealed that caspase-8 activity increased as expected M1 < M10 < M100 (Fig. 7).

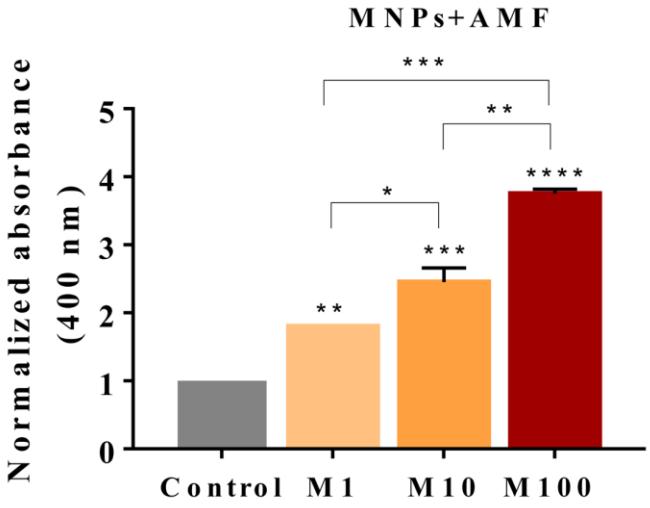

Figure 7. Analysis of the caspase-8 activity involved in the extrinsic cell death apoptotic pathways in three of the different models studied that evidence differences in the BAX/BCL-2 expression. Statistical significance between the means was determined using a one-way ANOVA followed of Tukey's multiple comparisons test (****$p < 0.0001$; ***$p < 0.001$; **$p < 0.01$; *$p \leq 0.05$; $p > 0.05$ no significance) comparing with the control group (0.0 μFe). In cases where more than one group generated significant differences with respect to control, the means between those groups were also compared.

As described before, following the activation of caspase-8, two possible routes could be followed: the continuation of the extrinsic pathway, or the initiation of the intrinsic pathway through BID, but in this case the BCL-2 family proteins would also be implicated resulting in an increase in the ratio *Bax*/*Bcl-2*. To further verify that the intrinsic pathway was not triggered through BID for the models containing the highest amount of intracellular MNPs, *Bid* expression was analyzed for M1, M10 and M100 samples. Following the same trend as *Bax*/*Bcl2* ratio, a reduction of the *Bid* expression was observed for increasing concentrations of MNPs (+AMF), suggesting that the extrinsic pathway was favored in the case of the highest intracellular MNP concentrations (Supporting information, Fig, S5).

Cell death mechanisms cannot be treated as exclusive, and it seems reasonable to consider that a specific stimulus could trigger a mixture of events. However, comparing all these results we observed a detectable tendency in triggering mainly an intrinsic or extrinsic mechanism depending on the MNP amount. As mentioned before, for the model with the lowest MNP content (M1) the increase in apoptosis was in total agreement with the increase of the ratio *Bax*/*Bcl-2*, indicating that, at these MNP levels, after the MH treatment the mechanism triggered was mainly intrinsic apoptosis. However, in cell models from M10 to M100, where a significant number of cells containing MNPs was achieved together with a significant decrease on the cell viability, very low levels of *Bax* and *Bcl-2* mRNA expression were observed. The increase of the activity of the caspase-8 indicated that for these higher MNP amounts, triggering of the extrinsic mechanism occurs during the MH treatment.

These results indicated that depending on the amount of MNPs internalized, different apoptotic pathways were triggered in response to the MH treatment. Nevertheless, as seen in the computational simulations, the important parameter to focus in was not only the number of particles internalized, but also the size of the vesicles they were entrapped, as this parameter had an important influence on the thermal effects. One possible hypothesis would be that the different apoptotic pathways triggered by the MH treatment could be related to the total or partial permeabilization of the lysosomal membrane, as it was previously demonstrated by other authors.[19-20] Our results also suggested a possible relationship between the apoptotic pathway triggered during the MH treatment and the size of the lysosomes containing the particles. Further experiments aiming to control the lysosome size would be helpful to verify this hypothesis.

These results are also especially relevant when designing the MH treatment, especially regarding the time elapsed between the MNPs administration and the AMF application. Time fluctuations on the number of MNPs per cell related to different processes such as the MNPs degradation,[63] the effect of cycles of endocytosis and exocytosis [64] or even the possible re-synthesis of de novo nanoparticles [65-66] may have an important effect on the cell death mechanism triggered causing variability on the treatment efficacy.

Finally, our observations open the way for future studies using different cell lines, specially cancer cell lines. The impact that the properties of the lysosomes (both size and membrane characteristics) from different cell lines may have on the response to the heat produced by the MNPs will be of special relevance to advance on the therapeutic outcomes of the MH treatment.

Conclusions

We established a series of 3D cell culture models containing different amounts of internalized MNPs. These models were of extreme use for the evaluation of the impact of the amount of intracellular MNPs on the death mechanisms triggered after a MH treatment.

Theoretical calculations indicated a large SAR drop after cell internalization, primarily due to the different field conditions. Additionally, a simple estimation suggested that a correlation between the number of particles and size of the vesicles where the particles are trapped after their internalization might result in different localized thermal effects, particularly due to the different energy density per surface area through the vesicles containing the MNPs' membrane. In contrast, the global cell temperature may not increase significantly.

Flow cytometry and *Bax* and *Bcl-2* mRNA levels showed that, although internalization of the MNPs did not lead to observable toxicity, there was an overexpression of the anti-apoptotic gene *Bcl-2*, which might be related to a protection mechanism.[67] At the highest concentrations of MNPs (M75 and M100), a slight cytotoxic effect could be observed. However, when exposing cells to the AMF, the amount of internalized MNPs was the key factor triggering different apoptotic routes.

Results indicated that, at the lowest concentrations, the apoptotic mechanism was mainly intrinsic. However, when increasing the amount of MNPs the intrinsic pathway became less important and the extrinsic pathway played a fundamental role on the cell death.

All together, these results are of great importance in the field of magnetic hyperthermia and for the support of MH as antitumoral treatment. In fact, our data clearly show that depending on the amount of internalized MNPs, the cell death mechanism is different as well as the subsequent biological events triggered. Modulating the amount of MNPs is a fundamental parameter to modulate the death pathway triggered during the MH and this would be a key tool when facing

preclinical experiments to ensure the real effectiveness of this therapeutic approach before effective translation to the clinic.

Materials & Methods

Magnetic Nanoparticles: synthesis, functionalization and characterization

Superparamagnetic iron oxide nanoparticles with an average size of around 11 nm were synthesized by thermal decomposition in organic medium. Then, the magnetic cores were transferred to aqueous medium (PMAO-TAMRA (carboxytetramethylrhodamine)) and functionalized with glucose based on a previously reported method.[9] Finally, MNPs were resuspended in phosphate-buffered saline buffer (PBS) and filtered with a syringe filter with a pore size of 0.22 μm (Merck Millipore, Darmstadt, Germany) to guarantee their sterility. Iron concentration was determined using a standard colorimetric procedure based on the use of 4,5-dihydroxy-1,3-benzenedisulfonic acid disodium salt monohydrate (Tiron).[3] Sample absorbance (480 nm) was measured on an UV-Vis spectrophotometer (Thermo Scientific Multiskan GO MA, USA) and compared to a calibration curve. An electrophoresis agarose gel 1% 0.5 Tris-borate-EDTA (TBE) was performed in order to corroborate the efficacy of the functionalization. The electrophoresis was performed at 90 V during 30 min. After this time, the gel was scanned with a Bio-Rad Gel Doc EZ equipment and the quotient of the migration distances of the MNPs samples before and after of the glucose functionalization was determined as quality control of the procedure. The image analysis of the agarose gel was performed with Gel Analyzer 2010 Program. Particle size and morphology were studied by transmission electron microscopy (TEM) using a Tecnai T20 (FEI company, OR, USA) microscope operating at 200 kV. The sample was prepared by placing a drop of a diluted suspension of the MNPs in water onto a carbon coated grid and

allowing it to dry. Particle size was determined by manual measurement of around 200 particles per sample using the Digital Micrograph software. The magnetic heating capacity of the MNPs was determined using a commercial alternating magnetic field generator (DM100; Nanoscale Biomagnetics, Spain). A 1 mg Fe/mL MNP sample was placed in a closed container centered in the inductive coil. The AMF was applied for 5 min using a field amplitude of H = 20.10 kA/m and a frequency of 829 kHz, while the temperature was recorded using an optic fiber sensor incorporated in the equipment. For the magnetic characterization, the MNPs liquid sample was allowed to dry at room temperature deposited into a piece of cotton wool that was subsequently placed into a gelatin capsule. Field dependent magnetization measurements were performed in a Quantum Design (USA) MPMS-XL SQUID magnetometer at 300 K with a maximum field of 5 T. Dynamic light scattering (DLS) was measured in Milli-Q water on a Malvern Zetasizer Nano-ZS, using ten runs per measurement and five replicates at 25 °C and pH 7. MNPs prepared to a final concentration of 0.1 mg/mL were incubated at room temperature with different biological media (cell culture medium with serum, cell culture medium without serum and PBS 1x) using 96-well plates. After 24 h, the samples were observed under optical microscope (Nikon Eclipse, TE2000-S) to observe the aggregation effects.

Cell culture

The murine macrophage RAW−264.7 cell line (ATCC® TIB71) was cultured and maintained in complete Dulbecco's Modified Eagle's Medium GlutaMAX™ Supplement (cDMEM; Gibco®, Thermo Fisher Scientific) supplemented with 10 % fetal bovine serum (FBS, Invitrogen), 100 U/mL penicillin G (sodium salt) and 100 µg/mL streptomycin sulfate (Invitrogen) at 37 °C in a humidified atmosphere at 5 % CO_2. Every four or five days in dependence of the confluency, the cell culture was diluted to 1:10. To detach the cells, these were incubated with Trypsin EDTA

solution (Sigma Aldrich) for 4 minutes at 37 ºC, in order to increase the viability. Then, the cells were scraped from the flask. Finally, cells were collected in fresh cDMEM.

To prepare the 3D cell culture models, the cells in suspension were incubated with different amounts of MNPs (1 µg; 10 µg; 25 µg; 50 µg; 75 µg and 100 µg of Fe) during 1 h at 37 ºC in 0.5 mL of cDMEM. After the incubation time, the medium with MNPs was discarded and the cells washed by centrifugation (300 xg, 5 min) twice. At this stage, iron quantification and MNPs internalization by fluorescence imagining were performed.

In order to perform the 3D cell cultures, the same procedure described before was performed, adding an extra step after removing the non-internalized particles through the washing by centrifugation in which the cells were mixed with the collagen gel. Just after the collagen gelling, 0.5 mL of cDMEM were added to the gel.[9] Cells were allowed to adjust to the 3D matrix during 1 h before performing the MH experiment.

Cellular localization and uptake quantification of MNPs

A Zeiss LSM 880 confocal microscope with a 63x/1.40 PlanApochromat objective was used to visualize MNPs localization in the 3D cell culture. The gels were fixed during 20 min with 0.5 mL of paraformaldehyde (4%). Then, the nuclei were stained with DAPI (4′,6-diamidino-2-phenylindole) and the cytoskeleton with Phalloidin488. The laser sources used were 458 nm, 488 nm (Argon Ion), and 561 nm (DPSS; Diode-pumped solid state). ZEN Microscope and Imaging Software was used for the image analysis.

Bright field and fluorescence images of cells incubated with the MNPs, before collagen gel formation, were carried out by observing the cells, adhered to 35 mm petri dishes, under an inverted fluorescence Olympus Ix81 microscope.

Flow cytometry and Inductively Coupled Plasma Optical Emission Spectrometry (ICP-OES) were used to determine the MNPs uptake and intracellular concentration, respectively. For the sample preparation, the same incubation protocols as described above were followed. For ICP-OES, cells were analyzed after the washing step to remove the unbound particles and before the preparation of the 3D structures. In the flow cytometry studies, cells were released from the 3D cell cultures [9] , and at a concentration of $2.5x10^4$ cells/mL resuspended in PBS were analyzed using the FL2 channel at 575 nm (Gallios™ Flow Cytometer, Beckman Coulter). For the ICP-OES studies, cell pellets from the different incubations were digested by heating with HNO_3 (Panreac) and then with H_2O_2 (Panreac) (both steps at 90 °C and during 1 h each). Finally, the samples were diluted until a final volume of 10 mL with MiliQ water and the concentration was determined using the Thermo Elemental IRIS Intrepid ICP-OES.

AC magnetic susceptibility measurements were performed in a Quantum Design (USA) MPMS-XL SQUID magnetometer using an AC amplitude of 0.41 Oe and a frequency of 11 Hz in the temperature range between 10 and 300 K. Freeze-dried cell pellets of around $3.5x10^5$ cells were placed into gelatin capsules for the measurements. The MNPs used for the quantification protocol were prepared in two different ways. One sample was prepared by placing a known volume of the original MNPs suspension into a cotton wool piece and another sample was diluted in a hot agar solution and maintained immersed in an ultrasound bath during the cooling down process to achieve a homogeneous dispersion of the particles within the sample and therefore reduce the interparticle dipolar interactions.

Magnetic hyperthermia treatment

3D cell cultures were thermalized at 37 °C using a water bath pump (Stryker - Medical Devices & Equipment Manufacturing Company) connected to a water tubing jacket. Then, the cell cultures

were exposed to an AMF (DM3, nB nanoscale Biomagnetics, Zaragoza, Spain) during 30 min. The frequency used was 337 kHz and the field amplitude of 13 kA/m.

Cell death studies

Cells were released from the 3D cell cultures [9] and re-suspended in 1X Annexin V Binding Buffer (10 mM HEPES/NaOH (pH=7.4) 140 mM NaCl, 2.5 mM $CaCl_2$) at a concentration of $1x10^6$ cells/mL. Then, 5 µl of Annexin V-FITC (Fluorescein Isothiocyanate) and 5 µL of Propidium Iodide (PI) were added to 100 µL of cell suspension and incubated at room temperature for 15 minutes in the dark (FITC-Annexin V Apoptosis Detection Kit). After the incubation period, 400 µL of 1X Annexin binding buffer was added and the sample was analyzed by flow cytometry. All samples were analyzed in a Gallios™ Flow Cytometer (Beckman Coulter) and the data interpreted with Kaluza 2.1 Software (Beckman Coulter).

Computational details

The thermal fluctuation and external field driven magnetisation behaviour of interacting magnetic particles was modelled by using kinetic Monte-Carlo approach.[49, 68] The model described in ref. [49] is based on the following system energy:

$$E = \sum \left(-K_i V_i \left(\hat{k}_i \cdot \hat{m}_i \right)^2 - M_s V \hat{m}_i \cdot \left(\vec{H}_{app} + \vec{H}_i^{mag} \right) \right) \quad (1)$$

with V_i being the volume of a particle *i*; M_s the saturation magnetisation; and $\hat{k}_i$ and $\hat{m}_i$ the anisotropy vector and magnetisation moment, respectively, both normalized to unity. The effective local field acting on particle *i* is given by the sum of the external applied field ($\vec{H}_{app}$) and the magnetostatic interaction field ($\vec{H}_i^{mag}$). The time dependent transition for a particle moment $\hat{m}_i$ to switch between the up ("1") and down ("2") states is:

$$P_i = 1 - exp(-t/\tau_i) \quad i = 1,2 \quad (2)$$

where the relaxation time constant τ_i is a reciprocal sum of the transition rates τ_i^+ and τ_i^- dependent on the energy barriers $\Delta E_i^{1,2}$ seen from the "1" and "2" states via the standard Neel-Arrhenius law:[69]

$$\tau_i^{1,2} = \tau_0 exp\left(\Delta E_i^{1,2}/k_B T\right) \quad (3)$$

where $\tau_0=10^{-9}$ s, k_B is the Boltzmann constant and T the temperature. The energy barrier, $\Delta E_i^{1,2}$, depends on the intrinsic particle properties, such as V_i and K_i.

The calculations were done considering log-normal distributions of anisotropy value of 10% and a 15% distribution in particle size. Example of the hysteresis loops for the in-water and *in vitro* conditions are shown in Figures S3 and S4 from the Supporting Information respectively. For the second case, the role of packing density was illustrated by considering packing densities between 2% and 40%.

RNA extraction and RT-PCR analysis

RNA was extracted from the same samples as described in the previous section. For this procedure, $2.5x10^5$ cells were centrifuged at 500 xg during 5 min at 4 ºC and the supernatant was discarded. The pellet was gently resuspended in 0.5 mL of Trisure (Bioline) and incubated 5 min at room temperature. After this time, 0.2 mL of chloroform were added and mixed vigorously during 15 min, then the solution was centrifuged to 12000 xg during 5 min and the upper aqueous phase was transferred to a new tube. Ice-cold isopropanol was added in a ratio of 1: 2.5 with respect to the volume recovered and incubated during 10 min to 4 ºC. The solution was centrifuged to 12000 xg, during 5min at 4 ºC, and the supernatant was discarded. The pellet was washed with 0.5 mL of ethanol 75 % (v/v), mixed using a vortex and then centrifuged at 7500 xg during 5 min. Finally, the supernatant was discarded and the pellet dried. For the quantification, the samples were resuspended in 0.05 mL of ultrapure water using a tip with filter.

For the RT-PCR studies, 350 ng of total RNA in each sample were reverse-transcribed into first-strand cDNA using NZY M-MuLV First-Strand cDNA Synthesis Kit. Five reactions were prepared (using flame) in dependence of the mRNA volume needed. The final volume was 10 µL. RNA samples were added and gently mixed with the reaction components (out of the flame area) and incubated in the thermocycler with the following program[70]: 1) 25 °C for 10 min; 2) 37 °C for 50 min; 3) 85 °C for 5 min. Then,1 µL of NZY RNase H (*E. coli*) was added to the reaction mix, that was incubated in the thermocycler to 37 °C during 20 min. cDNA obtained was used as template for the qPCR amplification. The qPCR was performed on a Corbett Rotor-Gene 6000 thermal cycler (QIAGEN) using the NZY qPCR Green Master Mix (2x) with the following primers, at a concentration of 0.1 µM each: *Bax* forward (5′-TGGCAGTGACATGTTTTCTGAC-3′) and *Bax* reverse (5′-TCACCCAACCACCCTGGT CTT-3′); *Bcl-2* forward (5′-CTTCGCCGAGATGTCCAGCCA-3′) and *Bcl-2* reverse (5′-GCTCTCCACACACATGACCC-3′); *18S* forward (5′-GTAACCCGTTGAACCCCATT-3′) and *18S* reverse (5′-CCATCCAATCGGTAGTAGCG-3′); *Bid* forward (5'-CTTGCTCCGTGATGTCTTTC-3') and *Bid* reverse (5'-TCCGTTCAGTCCATCCCATTT-3').[70-71] qPCR conditions included an initial denaturation at 95 ^{0}C for 10 min and 40 cycles of 95 ^{0}C for 20 s, 55 ^{0}C (*18S* and *Bid*) or 65 ^{0}C (*Bcl-2* and *Bax*) for 20 s, and 72 ^{0}C for 30 s (18S) or 20 s (*Bcl-2* and *Bax*). qPCR data were analyzed by the Ct method ($2^{-\Delta\Delta Ct}$),[72] where relative gene expression is given by quantification of the gene of interest (*Bid*, *Bax* or *Bcl-2*) relative to internal control gene (RNA*18S*), normalized to the control condition (non-treated cells).

caspase-8 Assay

For protein extraction, 4x10^6 cells were centrifuged to 500 rcf during 5 min at 4 ºC and all the supernatant was removed. Then 0.1 mL of fresh cold lysis buffer (4 ºC) was added to each sample

to solubilize the pellet. The mix was incubated at -80 ºC overnight. After this time, samples were thawed gently on ice. To disrupt the cell membranes, cycles of ultrasound bath in ice cold water were made (6 cycles, 2 min 30 s, the samples were setting on ice during 30 s between each cycle). Finally, the samples were centrifuged to 5000 xg during 5 min at 4 ºC and the supernatant transferred to a clean tube for protein quantification using a colorimetric Bradford test. The levels of caspase-8 were further determined using a colorimetric test – caspase-8 Assay Kit (ab39700). For that 10 µL of 1M DTT stock solution was added to 1 mL of 2X Reaction Buffer (100 mM DTT final concentration) and 50 µL of 2X Reaction Buffer/DTT mixture was added into each reaction well containing 50 µg of protein (sample and background control wells). The solution was mixed well by pipetting up and down. Finally, 5 µL of IETD-pNA substrate (4M stock) was added into each well (200 mM final substrate concentration) and mix well by pipetting up and down. The plate was covered and incubated at 37 °C for 2 hours. After this time the absorbance was measured on a microplate reader at OD 400 nm.

Statistical Analysis

Data are expressed as mean ± SD of a minimum three biological replicas. Statistical significance of difference in means was performed using GraphPad Prism v7.00. One-way ANOVA tests were used for the analysis of the data. The confidence interval was 95%.

SUPPORTING INFORMATION

Figure S1. Characterization of the MNPs glucose functionalization efficacy

Figure S2. Cell viability studies.

Figures S3, S4 and associated text. Computational details

Figure S5. *Bid* expression analysis.

Author Contributions

L.B., L.A. V. G. and L. G. Designed the experiments. L.B., Y. F-A., C. R-R., R.M.F. Performed the experiments. L.B., L.A., A. R. F., P.V. B., J. M. F., V. G. and L. G. Analyzed experimental data and discussed the results. D. S., S. R and R. W.C. Performed the computational analysis. The manuscript was written through contributions of all authors. All authors gave approval to the final version of the manuscript.

ACKNOWLEDGMENT

This work was funded by the European Commission through the M-ERA.NET COFUND Project MagicCellGene (PCIN-2017-060, FCT/MCTES M-ERA NET/2/0008/2016), Spanish MCIU (PGC2018-096016-B-I00 to R.M.F and L.G. and BIO2017-84246-C2-1-R to J.M.F. and V.G.), the Applied Molecular Biosciences Unit - UCIBIO which is financed by national funds from FCT (UIDB/04378/2020) and Fondo Social de la DGA (grupos DGA). L.B and Y.F-A. thanks Santander-Universidad Zaragoza Fellowship program for their PhD fellowships. D.S acknowledges Xunta de Galicia for financial support under the I2C Plan and the Strategic Grouping in Materials (AeMAT; grant No. ED431E2018/08). This work made use of computational facilities funded by the Small items of research equipment at the University of York ENERGY (Grant No. EP/K031589/1). L.B. acknowledges support from Santander Universidad and Erasmus Campus Iberus to perform experimental work at Universidade Nova de Lisboa. L.A. acknowledges support from the José Castillejo program (CAS18/00233). L.G. and R.M.F.

acknowledge financial support from the Ramón y Cajal program (RYC-2014-15512 and RYC-2015-17640). The authors would like to acknowledge the use of Servicios Científicos Técnicos del CIBA (IACS-Universidad de Zaragoza), the Advanced Microscopy Laboratory (INA-Universidad de Zaragoza), for access to their instrumentation and expertise and Servicio General de Apoyo a la Investigación-SAI, Universidad de Zaragoza.

References

1. Beik, J.; Abed, Z.; Ghoreishi, F. S.; Hosseini-Nami, S.; Mehrzadi, S.; Shakeri-Zadeh, A.; Kamrava, S. K., Nanotechnology in Hyperthermia Cancer Therapy: From Fundamental Principles to Advanced Applications. *J Control Release* **2016,** *235*, 205-221.

2. Dutz, S.; Hergt, R., Magnetic Nanoparticle Heating and Heat Transfer on a Microscale: Basic Principles, Realities and Physical Limitations of Hyperthermia for Tumour Therapy. *Int J Hyperthermia* **2013,** *29* (8), 790-800.

3. Dias, J. T.; Moros, M.; Del Pino, P.; Rivera, S.; Grazu, V.; de la Fuente, J. M., DNA as a Molecular Local Thermal Probe for the Analysis of Magnetic Hyperthermia. *Angew Chem Int Ed Engl* **2013,** *125*(44), 11740-117439.

4. Riedinger, A.; Guardia, P.; Curcio, A.; Garcia, M. A.; Cingolani, R.; Manna, L.; Pellegrino, T., Subnanometer Local Temperature Probing and Remotely Controlled Drug Release Based on Azo-Functionalized Iron Oxide Nanoparticles. *Nano Lett* **2013,** *13* (6), 2399-2406.

5. Shi, L.; Dames, C.; Lukes, J. R.; Reddy, P.; Duda, J.; Cahill, D. G.; Lee, J.; Marconnet, A.; Goodson, K. E.; Bahk, J.-H., Evaluating Broader Impacts of Nanoscale Thermal Transport Research. *Nanosc Microsc Therm* **2015,** *19* (2), 127-165.

6. Garanina, A. S.; Naumenko, V. A.; Nikitin, A. A.; Myrovali, E.; Petukhova, A. Y.; Klimyuk, S. V.; Nalench, Y. A.; Ilyasov, A. R.; Vodopyanov, S. S.; Erofeev, A. S., Temperature-Controlled Magnetic Nanoparticles Hyperthermia Inhibits Primary Tumor Growth and Metastases Dissemination. *Nanomed- Nanotechnol* **2020,** *25*, 102171.

7. Asin, L.; Goya, G.; Tres, A.; Ibarra, M., Induced Cell Toxicity Originates Dendritic Cell Death Following Magnetic Hyperthermia Treatment. *Cell death & dis* **2013,** *4* (4), e596-e596.

8. Asín, L.; Ibarra, M. R.; Tres, A.; Goya, G. F., Controlled Cell Death by Magnetic Hyperthermia: Effects of Exposure Time, Field Amplitude, and Nanoparticle Concentration. *Pharm. Res.* **2012,** *29* (5), 1319-1327.

9. Beola, L.; Asín, L.; Fratila, R. M.; Herrero, V.; de la Fuente, J. M.; Grazú, V.; Gutiérrez, L., Dual Role of Magnetic Nanoparticles as Intracellular Hotspots and Extracellular Matrix Disruptors Triggered by Magnetic Hyperthermia in 3d Cell Culture Models. *ACS Appl Mater Interfaces* **2018,** *10* (51), 44301-44313.

10. Marcos-Campos, I.; Asin, L.; Torres, T.; Marquina, C.; Tres, A.; Ibarra, M.; Goya, G., Cell Death Induced by the Application of Alternating Magnetic Fields to Nanoparticle-Loaded Dendritic Cells. *Nanotechnology* **2011,** *22* (20), 205101.

11. Moros, M.; Ambrosone, A.; Stepien, G.; Fabozzi, F.; Marchesano, V.; Castaldi, A.; Tino, A.; de la Fuente, J. M.; Tortiglione, C., Deciphering Intracellular Events Triggered by Mild Magnetic Hyperthermia in Vitro and in Vivo. *Nanomedicine* **2015,** *10* (14), 2167-2183.

12. Liu, Q.; Huang, J.; Feng, Q.; Zhang, T.; Chen, X.; Li, X.; Liu, X.; Li, H.; Zhong, Z.; Xiao, K., Multi-Modal Visualization of Uptake and Distribution of Iron Oxide Nanoparticles in Macrophages, Cancer Cells, and Xenograft Models. *J Biomed Nanotech* **2019,** *15* (8), 1801-1811.

13. Raj, D. B. T. G.; Khan, N. A., Surface Functionalization Dependent Subcellular Localization of Superparamagnetic Nanoparticle in Plasma Membrane and Endosome. *Nano converg* **2018,** *5* (1), 4.

14. Raj, D. B. T. G.; Khan, N. A.; Venkatachalam, S.; Chu, D. T.; Arumugam, S., Step-by-Step Protocol for Superparamagnetic Nanoparticle-Based Endosome and Lysosome Isolation from Eukaryotic Cell. In: Turksen K. (eds) Stem Cell Nanotechnology. Methods in Molecular Biology, vol 2125. Humana, New York, NY. **2019**, 167-172.

15. Di Corato, R.; Espinosa, A.; Lartigue, L.; Tharaud, M.; Chat, S.; Pellegrino, T.; Ménager, C.; Gazeau, F.; Wilhelm, C., Magnetic Hyperthermia Efficiency in the Cellular Environment for Different Nanoparticle Designs. *Biomaterials* **2014,** *35* (24), 6400-6411.

16. Mukherjee, A.; Castanares, M.; Hedayati, M.; Wabler, M.; Trock, B.; Kulkarni, P.; Rodriguez, R.; Getzenberg, R. H.; DeWeese, T. L.; Ivkov, R., Monitoring Nanoparticle-Mediated Cellular Hyperthermia with a High-Sensitivity Biosensor. *Nanomedicine* **2014,** *9* (18), 2729-2743.

17. Creixell, M.; Bohorquez, A. C.; Torres-Lugo, M.; Rinaldi, C., Egfr-Targeted Magnetic Nanoparticle Heaters Kill Cancer Cells without a Perceptible Temperature Rise. *ACS nano* **2011,** *5* (9), 7124-7129.

18. Rodriguez-Luccioni, H. L.; Latorre-Esteves, M.; Méndez-Vega, J.; Soto, O.; Rodríguez, A. R.; Rinaldi, C.; Torres-Lugo, M., Enhanced Reduction in Cell Viability by Hyperthermia Induced by Magnetic Nanoparticles. *Int J Nanomedicine* **2011,** *6*, 373-380.

19. Domenech, M.; Marrero-Berrios, I.; Torres-Lugo, M.; Rinaldi, C., Lysosomal Membrane Permeabilization by Targeted Magnetic Nanoparticles in Alternating Magnetic Fields. *ACS nano* **2013,** *7* (6), 5091-5101.

20. Clerc, P.; Jeanjean, P.; Hallali, N.; Gougeon, M.; Pipy, B.; Carrey, J.; Fourmy, D.; Gigoux, V., Targeted Magnetic Intra-Lysosomal Hyperthermia Produces Lysosomal Reactive Oxygen Species and Causes Caspase-1 Dependent Cell Death. *J Control Release* **2018,** *270*, 120-134.

21. Guicciardi, M. E.; Leist, M.; Gores, G. J., Lysosomes in Cell Death. *Oncogene* **2004,** *23* (16), 2881-2890.

22. Kirkegaard, T.; Jäättelä, M., Lysosomal Involvement in Cell Death and Cancer. *Bba-Mol Cell Res* **2009,** *1793* (4), 746-754.

23. Turk, B.; Stoka, V.; Rozman-Pungercar, J.; Cirman, T.; Droga-Mazovec, G.; Oreic, K.; Turk, V., Apoptotic Pathways: Involvement of Lysosomal Proteases. *Biol Chem* **2002,** *383* (7-8), 1035-1044.

24. P Calatayud, M.; Asin, L.; Tres, A.; F Goya, G.; R Ibarra, M., Cell Bystander Effect Induced by Radiofrequency Electromagnetic Fields and Magnetic Nanoparticles. *Curr Nanosci* **2016,** *12* (3), 372-377.

25. Lee, Y.; Overholtzer, M., Focus: Death: After-Death Functions of Cell Death. *YJBM* **2019,** *92* (4), 687-694.

26. Acebes-Huerta, A.; Lorenzo-Herrero, S.; Folgueras, A. R.; Huergo-Zapico, L.; Lopez-Larrea, C.; López-Soto, A.; Gonzalez, S., Drug-Induced Hyperploidy Stimulates an Antitumor Nk Cell Response Mediated by Nkg2d and Dnam-1 Receptors. *Oncoimmunology* **2016,** *5* (2), e1074378.

27. Galluzzi, L.; Buqué, A.; Kepp, O.; Zitvogel, L.; Kroemer, G., Immunogenic Cell Death in Cancer and Infectious Disease. *Nat Rev Immunol* **2017,** *17* (2), 97-111.

28. Tambe, D. T.; Hardin, C. C.; Angelini, T. E.; Rajendran, K.; Park, C. Y.; Serra-Picamal, X.; Zhou, E. H.; Zaman, M. H.; Butler, J. P.; Weitz, D. A.; Fredberg, J. J.; Trepat, X., Collective Cell Guidance by Cooperative Intercellular Forces. *Nat Mater* **2011,** *10* (6), 469-475.

29. Moros, M.; Hernáez, B.; Garet, E.; Dias, J. T.; Sáez, B.; Grazú, V.; González-Fernández, A. f.; Alonso, C.; de la Fuente, J. s. M., Monosaccharides Versus Peg-Functionalized Nps: Influence in the Cellular Uptake. *ACS nano* **2012,** *6* (2), 1565-1577

30. Macheda, M. L.; Rogers, S.; Best, J. D., Molecular and Cellular Regulation of Glucose Transporter (Glut) Proteins in Cancer. *J. Cell. Physiol.* **2005,** *202* (3), 654-662.

31. Prasad, N.; Rathinasamy, K.; Panda, D.; Bahadur, D., Mechanism of Cell Death Induced by Magnetic Hyperthermia with Nanoparticles of Γ-Mn X Fe 2–X O 3 Synthesized by a Single Step Process. *J Mater Chem* **2007,** *17* (48), 5042-5051.

32. Blanco-Andujar, C.; Ortega, D.; Southern, P.; Nesbitt, S. A.; Thanh, N. T. K.; Pankhurst, Q. A., Real-Time Tracking of Delayed-Onset Cellular Apoptosis Induced by Intracellular Magnetic Hyperthermia. *Nanomedicine* **2016,** *11* (2), 121-136.

33. Harunaga, J. S.; Yamada, K. M., Cell-Matrix Adhesions in 3d. *Matrix Biol* **2011,** *30* (7-8), 363-368.

34. Stocke, N. A.; Sethi, P.; Jyoti, A.; Chan, R.; Arnold, S. M.; Hilt, J. Z.; Upreti, M., Toxicity Evaluation of Magnetic Hyperthermia Induced by Remote Actuation of Magnetic Nanoparticles in 3d Micrometastasic Tumor Tissue Analogs for Triple Negative Breast Cancer. *Biomaterials* **2017,** *120*, 115-125.

35. Ruiz, A.; Alpízar, A.; Beola, L.; Rubio, C.; Gavilán, H.; Marciello, M.; Rodríguez-Ramiro, I.; Ciordia, S.; Morris, C. J.; Morales, M. d. P., Understanding the Influence of a Bifunctional Polyethylene Glycol Derivative in Protein Corona Formation around Iron Oxide Nanoparticles. *Materials* **2019,** *12* (14), 2218.

36. Stone, L., Prostate Cancer: A Glitch in the Extracellular Matrix. *Nat. Rev. Urol.* **2016,** *14* (1), 1759-4820.

37. Ioachim, E.; Charchanti, A.; Briasoulis, E.; Karavasilis, V.; Tsanou, H.; Arvanitis, D. L.; Agnantis, N. J.; Pavlidis, N., Immunohistochemical Expression of Extracellular Matrix Components Tenascin, Fibronectin, Collagen Type Iv and Laminin in Breast Cancer: Their

Prognostic Value and Role in Tumour Invasion and Progression. *Eur J Cancer* **2002,** *38* (18), 2362-2370

38. Netti, P. A.; Berk, D. A.; Swartz, M. A.; Grodzinsky, A. J.; Jain, R. K., Role of Extracellular Matrix Assembly in Interstitial Transport in Solid Tumors. *Cancer Res* **2000,** *60* (9), 2497-2503.

39. Moore, A.; Weissleder, R.; Bogdanov Jr, A., Uptake of Dextran-Coated Monocrystalline Iron Oxides in Tumor Cells and Macrophages. *J. Magn Reson Imaging* **1997,** *7* (6), 1140-1145.

40. Rojas, J. M.; Sanz-Ortega, L.; Mulens-Arias, V.; Gutierrez, L.; Perez-Yague, S.; Barber, D. F., Superparamagnetic Iron Oxide Nanoparticle Uptake Alters M2 Macrophage Phenotype, Iron Metabolism, Migration and Invasion. *Nanomedicine_UK* **2016,** *12* (4), 1127-1138.

41. Moros, M.; Ambrosone, A.; Stepien, G.; Fabozzi, F.; Marchesano, V.; Castaldi, A.; Tino, A.; de la Fuente, J. M.; Tortiglione, C., Deciphering Intracellular Events Triggered by Mild Magnetic Hyperthermia in Vitro and in Vivo. *Nanomedicine* **2015,** *10* (14), 2167-2183

42. Wlodkowic, D.; Skommer, J.; Darzynkiewicz, Z., Flow Cytometry-Based Apoptosis Detection. *Methods Mol Biol* **2009,** *559*, 19-32.

43. Sanz, B.; Calatayud, M. P.; Torres, T. E.; Fanarraga, M. L.; Ibarra, M. R.; Goya, G. F., Magnetic Hyperthermia Enhances Cell Toxicity with Respect to Exogenous Heating. *Biomaterials* **2017,** *114*, 62-70.

44. Coral, D. F.; Mendoza Zelis, P.; Marciello, M.; Morales, M. a. d. P.; Craievich, A.; Sánchez, F. H.; Fernández van Raap, M. B., Effect of Nanoclustering and Dipolar Interactions in Heat Generation for Magnetic Hyperthermia. *Langmuir* **2016,** *32* (5), 1201-1213.

45. Serantes, D.; Baldomir, D.; Martinez-Boubeta, C.; Simeonidis, K.; Angelakeris, M.; Natividad, E.; Castro, M.; Mediano, A.; Chen, D.-X.; Sanchez, A., Influence of Dipolar Interactions on Hyperthermia Properties of Ferromagnetic Particles. *J Appl Phys* **2010,** *108* (7), 073918.

46. Munoz-Menendez, C.; Serantes, D.; Ruso, J. M.; Baldomir, D., Towards Improved Magnetic Fluid Hyperthermia: Major-Loops to Diminish Variations in Local Heating. *Phys Chem Chem Phys* **2017,** *19* (22), 14527-14532.

47. Conde-Leboran, I.; Baldomir, D.; Martinez-Boubeta, C.; Chubykalo-Fesenko, O.; del Puerto Morales, M.; Salas, G.; Cabrera, D.; Camarero, J.; Teran, F. J.; Serantes, D., A Single Picture Explains Diversity of Hyperthermia Response of Magnetic Nanoparticles. *J Phys Chem C* **2015,** *119* (27), 15698-15706.

48. Martinez-Boubeta, C.; Simeonidis, K.; Serantes, D.; Conde-Leborán, I.; Kazakis, I.; Stefanou, G.; Peña, L.; Galceran, R.; Balcells, L.; Monty, C., Adjustable Hyperthermia Response of Self-Assembled Ferromagnetic Fe-Mgo Core–Shell Nanoparticles by Tuning Dipole–Dipole Interactions. *Adv. Funct. Mater.* **2012,** *22* (17), 3737-3744.

49. Ruta, S.; Chantrell, R.; Hovorka, O., Unified Model of Hyperthermia Via Hysteresis Heating in Systems of Interacting Magnetic Nanoparticles. *Sci Rep* **2015,** *5*, 9090.

50. Vallejo-Fernandez, G.; O'Grady, K., Effect of the Distribution of Anisotropy Constants on Hysteresis Losses for Magnetic Hyperthermia Applications. *Appl Phys Lett* **2013,** *103* (14), 142417.

51. Martinez-Boubeta, C.; Simeonidis, K.; Makridis, A.; Angelakeris, M.; Iglesias, O.; Guardia, P.; Cabot, A.; Yedra, L.; Estradé, S.; Peiró, F., Learning from Nature to Improve the Heat Generation of Iron-Oxide Nanoparticles for Magnetic Hyperthermia Applications. *Sci Rep* **2013,** *3*, 1652.

52. Etheridge, M. L.; Hurley, K. R.; Zhang, J.; Jeon, S.; Ring, H. L.; Hogan, C.; Haynes, C. L.; Garwood, M.; Bischof, J. C., Accounting for Biological Aggregation in Heating and Imaging of Magnetic Nanoparticles. *Technology* **2014,** *2* (03), 214-228.

53. Soukup, D.; Moise, S.; Céspedes, E.; Dobson, J.; Telling, N. D., In Situ Measurement of Magnetization Relaxation of Internalized Nanoparticles in Live Cells. *ACS nano* **2015,** *9* (1), 231-240.

54. Moise, S.; Céspedes, E.; Soukup, D.; Byrne, J. M.; El Haj, A. J.; Telling, N. D., The Cellular Magnetic Response and Biocompatibility of Biogenic Zinc-and Cobalt-Doped Magnetite Nanoparticles. *Sci Rep* **2017,** *7*, 39922.

55. Cabrera, D.; Coene, A.; Leliaert, J.; Artés-Ibáñez, E. J.; Dupré, L.; Telling, N. D.; Teran, F. J., Dynamical Magnetic Response of Iron Oxide Nanoparticles inside Live Cells. *ACS nano* **2018,** *12* (3), 2741-2752.

56. Andrä, W.; d'Ambly, C.; Hergt, R.; Hilger, I.; Kaiser, W., Temperature Distribution as Function of Time around a Small Spherical Heat Source of Local Magnetic Hyperthermia. *J Magn Magn Mater* **1999,** *194* (1-3), 197-203.

57. McHale, G.; Newton, M., Liquid Marbles: Topical Context within Soft Matter and Recent Progress. *Soft Matter* **2015,** *11* (13), 2530-2546.

58. Fox, J. L.; MacFarlane, M., Targeting Cell Death Signalling in Cancer: Minimising 'Collateral Damage'. *Br J Cancer* **2016,** *115* (1), 5-11.

59. Goldar, S.; Khaniani, M. S.; Derakhshan, S. M.; Baradaran, B., Molecular Mechanisms of Apoptosis and Roles in Cancer Development and Treatment. *Asian Pac J Cancer Prev* **2015,** *16* (6), 2129-2144.

60. Johansson, A.-C.; Appelqvist, H.; Nilsson, C.; Kågedal, K.; Roberg, K.; Öllinger, K., Regulation of Apoptosis-Associated Lysosomal Membrane Permeabilization. *Apoptosis* **2010,** *15* (5), 527-540.

61. Stoka, V.; Turk, V.; Turk, B., Lysosomal Cysteine Cathepsins: Signaling Pathways in Apoptosis. *Biol Chem* **2007,** *388* (6), 555-560.

62. Raisova, M.; Hossini, A. M.; Eberle, J.; Riebeling, C.; Orfanos, C. E.; Geilen, C. C.; Wieder, T.; Sturm, I.; Daniel, P. T., The Bax/Bcl-2 Ratio Determines the Susceptibility of Human Melanoma Cells to Cd95/Fas-Mediated Apoptosis. *J Invest Dermatol* **2001,** *117* (2), 333-340.

63. Rojas, J. M.; Gavilan, H.; Del Dedo, V.; Lorente-Sorolla, E.; Sanz-Ortega, L.; da Silva, G. B.; Costo, R.; Perez-Yague, S.; Talelli, M.; Marciello, M.; Morales, M. P.; Barber, D. F.; Gutierrez, L., Time-Course Assessment of the Aggregation and Metabolization of Magnetic Nanoparticles. *Acta Biomater* **2017,** *58*, 181-195.

64. Del Sol-Fernández, S.; Portilla-Tundidor, Y.; Gutiérrez, L.; Odio, O.; Reguera, E.; Barber, D. F.; Morales, M., Flower-Like Mn-Doped Magnetic Nanoparticles Functionalized with A V B3-Integrin-Ligand to Efficiently Induce Intracellular Heat after Alternating Magnetic Field

Exposition, Triggering Glioma Cell Death. *ACS Appl Mater Interfaces* **2019,** *11* (30), 26648-26663.

65. Curcio, A.; Van de Walle, A.; Serrano, A.; Prévéral, S.; Pechoux, C.; Pignol, D.; Menguy, N.; Lefevre, C. T.; Espinosa, A.; Wilhelm, C., Transformation Cycle of Magnetosomes in Human Stem Cells: From Degradation to Biosynthesis of Magnetic Nanoparticles Anew. *ACS nano* **2019,** *14* (2), 1406-1417.

66. Van de Walle, A.; Sangnier, A. P.; Abou-Hassan, A.; Curcio, A.; Hemadi, M.; Menguy, N.; Lalatonne, Y.; Luciani, N.; Wilhelm, C., Biosynthesis of Magnetic Nanoparticles from Nano-Degradation Products Revealed in Human Stem Cells. *Proc. Natl. Acad. Sci. U S A* **2019,** *116* (10), 4044-4053.

67. Galluzzi, L.; Vitale, I.; Aaronson, S. A.; Abrams, J. M.; Adam, D.; Agostinis, P.; Alnemri, E. S.; Altucci, L.; Amelio, I.; Andrews, D. W., Molecular Mechanisms of Cell Death: Recommendations of the Nomenclature Committee on Cell Death 2018. *Cell Death & Differ* **2018,** *25* (3), 486-541.

68. Chantrell, R.; Walmsley, N.; Gore, J.; Maylin, M., Calculations of the Susceptibility of Interacting Superparamagnetic Particles. *Phys Rev B* **2000,** *63* (2), 024410.

69. Néel, L., Théorie Du Traînage Magnétique Des Ferromagnétiques En Grains Fins Avec Applications Aux Terres Cuites. *Ann Géophys* **1949,** *5*, 99-136.

70. Martins, M.; Baptista, P. V.; Mendo, A. S.; Correia, C.; Videira, P.; Rodrigues, A. S.; Muthukumaran, J.; Santos-Silva, T.; Silva, A.; da Silva, M. F. C. G., In Vitro and in Vivo

Biological Characterization of the Anti-Proliferative Potential of a Cyclic Trinuclear Organotin (Iv) Complex. *Mol BioSyst* **2016,** *12* (3), 1015-1023.

71. Svahn, N.; Moro, A. J.; Roma-Rodrigues, C.; Puttreddy, R.; Rissanen, K.; Baptista, P. V.; Fernandes, A. R.; Lima, J. C.; Rodríguez, L., The Important Role of the Nuclearity, Rigidity, and Solubility of Phosphane Ligands in the Biological Activity of Gold (I) Complexes. *Chem Eur J* **2018,** *24* (55), 14654-14667.

72. Livak, K. J.; Schmittgen, T. D., Analysis of Relative Gene Expression Data Using Real-Time Quantitative Pcr and the 2− Δδct Method. *Methods* **2001,** *25* (4), 402-408.